

Pure Goldstone mode in the quench dynamics of a confined ultracold Fermi gas in the BCS-BEC crossover regime

P. Kettmann,¹ S. Hannibal,¹ M. D. Croitoru,² V. M. Axt,² and T. Kuhn¹

¹*Institut für Festkörperteorie, Westfälische Wilhelms-Universität Münster, 48149 Münster, Germany*

²*Theoretische Physik III, Universität Bayreuth, 95440 Bayreuth, Germany*

(Dated: July 12, 2021)

We present a numerical study of the dynamic response of a confined superfluid Fermi gas to a rapid change of the scattering length (i.e., an interaction quench). Based on a fully microscopic time-dependent density-matrix approach within the full Bogoliubov-de Gennes formalism that includes a 3D harmonic confinement we simulate and identify the emergence of a Goldstone mode of the BCS gap in a cigar-shaped ⁶Li gas. By analyzing this Goldstone mode over a wide range of parameters, we show that its excitation spectrum is gapless and that its main frequency is not fixed by the trapping potential but that it is determined by the details of the quench. Thus, we report the emergence of a pure Goldstone mode of the BCS gap that –in contrast to situations in many previous studies– maintains its gapless excitation spectrum predicted by the Goldstone theorem. Furthermore, we observe that the size-dependent superfluid resonances resulting from the atypical BCS-BEC crossover have a direct impact on this Goldstone mode. Finally, we find that the interaction quench-induced Goldstone mode leads to a low-frequency in-phase oscillation of the single-particle occupations with complete inversion of the lowest-lying single-particle states which could provide a convenient experimental access to the pure gapless Goldstone mode.

PACS numbers: 67.85.Lm, 67.85.De

Keywords: BCS, Ultracold Fermi gas, Bogoliubov-de Gennes equation, Goldstone mode

I. INTRODUCTION

Due to their unique controllability ultracold Fermi gases provide an ideal system to test concepts of many-particle physics as well as particle theory. Adjustable interparticle interactions provide the possibility to explore both the regime of weak attractive interactions where a superfluid Bardeen Cooper Schrieffer (BCS) phase emerges as well as the regime of weak repulsive interactions which lead to the formation of a Bose-Einstein condensate (BEC). Both regimes are connected by a smooth BCS-BEC crossover with strong interparticle interactions including a point of unitarity where the coupling strength diverges [1, 2]. Furthermore, the emergence of a BCS phase is associated with a spontaneously broken $U(1)$ symmetry which makes ultracold Fermi gases a convenient candidate to study the fundamental concept of spontaneous symmetry breaking (SSB) [3].

Spontaneously broken gauge symmetries and the resulting two types of fundamental collective excitations –gapped amplitude/Higgs modes and gapless phase/Goldstone modes (see Fig. 1)– are of fundamental interest for several fields of physics like condensed matter and particle physics. Probably the most prominent application of the concept of SSB is the Higgs mechanism in particle physics [4]. In condensed matter physics SSB occurs in several systems, for example in ferromagnets (see, e.g., [5]), superfluid ³He [6, 7] and BCS superconductors [3, 8]. In these cases, the fundamental excitations –known as magnons (i.e., spin waves), second sound (i.e., heat waves) and plasmons– correspond to the Goldstone modes resulting from SSB.

In the field of ultracold Fermi gases the Higgs and the

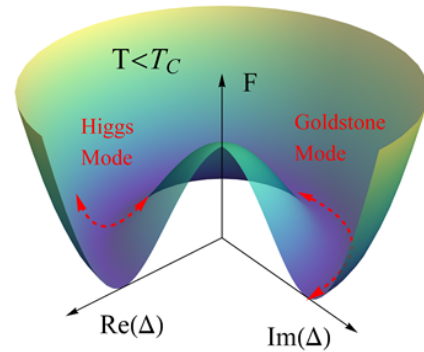


FIG. 1. (color online) Ginzburg-Landau free energy of a BCS phase of a homogeneous Fermi gas for $T < T_C$ (schematic). The rotational $U(1)$ symmetry is broken, when the gap Δ of the system gains a certain phase inside the rim of the potential. The resulting excitation modes are the Higgs-amplitude mode and the Goldstone mode, i.e., a phase oscillation of the gap.

Goldstone mode have received great attention over the past years. The Higgs mode, i.e., the amplitude oscillation of the BCS gap, is difficult to address in experiment since it does not couple directly to external probes [9]. This is why measurements of the Higgs mode have only recently been achieved for lattice superfluids [10, 11] (in the case of BCS superconductors an experimental access has been found via THz spectroscopy [12, 13]), while several theoretical studies on the Higgs mode have been reported [14–20]. In contrast, the Goldstone mode, i.e., the oscillation of the complex phase of the BCS gap, has been intensively studied both theoretically and experimentally

(see, e.g., [21–34]).

However, most previous studies were based on the fact that the Goldstone mode couples to the real-space dynamics of the Fermi gas. Therefore, it can be excited by inducing a collective oscillation of the trapped cloud, which can be achieved, e.g., by various schemes of confinement change or by optical excitation. The dynamics in the Goldstone mode is then directly reflected in the collective oscillation of the cloud and can be observed via the latter. However, a coupling to the real-space oscillation of the cloud implies a coupling to the trapping potential. I.e., in the previous studies the frequency of the Goldstone mode was fixed by the frequencies of the trap which stands in direct contrast to the Goldstone theorem predicting a gapless excitation spectrum of the phase mode. Thus, the observation of the gapless phase mode resulting from the Goldstone theorem was so far obstructed by the coupling to the trapping potential via the collective oscillation of the cloud.

In contrast, we report the emergence of a pure Goldstone mode in the dynamics of a trapped ultracold Fermi gas by showing that its original gapless excitation spectrum can be recovered by exciting the cloud via an interaction quench. To this end, we observe that the frequency of the interaction quench-induced phase mode can be tuned over a wide range from zero to finite values by adjusting the details of the quench. We explain this by the circumstance that the excited Goldstone mode is homogeneous, i.e., that it does not introduce any phase gradients, and that it therefore does not couple to the trapping potential.

To do so, we study the dynamics of the BCS gap of a confined ultracold ${}^6\text{Li}$ gas at $T = 0$ on the BCS side of the BCS-BEC crossover [i.e., the Fermi wave vector k_F times the scattering length a is given by $0 > 1/(k_F a) > -1$] as well as in the BCS regime [i.e., $-1 > 1/(k_F a)$]. We calculate the dynamics of the Bogoliubov quasiparticles in the framework of the Bogoliubov-de Gennes (BdG) formalism and by that the dynamics of the BCS gap. The investigated system is in the low-density regime, i.e., we use a short-range s-wave interaction between particles with opposite spin. The confinement is modeled by a cigar-shaped 3D harmonic potential, which in good approximation describes the standard laser confinement used in experiment [2]. The system is excited by an instantaneous interaction quench, i.e., a rapid change of the interparticle interaction strength. This can experimentally be achieved, e.g., by an optical control of a Feshbach resonance [35].

Our work is structured as follows. In section II we present the formalism we used within the context of this work, i.e., a full BdG approach as well as its simplification via the Anderson approximation. We will derive the equations of motion for the quasiparticle expectation values which allow for a calculation of the phase dynamics of the BCS gap. In section III we present the results obtained by the full BdG approach and show that they are well reproduced by Anderson’s approximate solution.

Based on the latter we will analyze the effect of the excitation parameters and of the trapping frequencies on the interaction-quench-induced Goldstone mode as well as the impact of this Goldstone mode on an experimentally accessible quantity, i.e., the single-particle excitations of the cloud. Finally, we conclude and summarize our findings in section IV.

II. THEORETICAL APPROACH

To calculate the ground state as well as the dynamical properties of a BCS condensate in a trap we start from the Bogoliubov-de Gennes (BdG) Hamiltonian [36, 37]:

$$H_{BdG} = \int \Psi_{\uparrow}^{\dagger}(\mathbf{r}) H_0 \Psi_{\uparrow}(\mathbf{r}) d^3r + \int \Psi_{\downarrow}^{\dagger}(\mathbf{r}) H_0 \Psi_{\downarrow}(\mathbf{r}) d^3r + \int \left[\Delta(\mathbf{r}) \Psi_{\uparrow}^{\dagger}(\mathbf{r}) \Psi_{\downarrow}^{\dagger}(\mathbf{r}) + \Delta^*(\mathbf{r}) \Psi_{\downarrow}(\mathbf{r}) \Psi_{\uparrow}(\mathbf{r}) \right] d^3r. \quad (1)$$

Here the field operators $\Psi_{\sigma}^{(\dagger)}(\mathbf{r})$ describe the annihilation (creation) of Fermions—in this case atoms of ${}^6\text{Li}$ —with spin σ at the position \mathbf{r} and the BCS gap is given by

$$\Delta(\mathbf{r}) = -g \langle \Psi_{\downarrow}(\mathbf{r}) \Psi_{\uparrow}(\mathbf{r}) \rangle. \quad (2)$$

The interaction strength $g = -\frac{4\pi\hbar^2 a}{m}$ is determined by the s-wave scattering length a and the mass of the particles m . The 3D harmonic trapping potential $V(\mathbf{r})$ is included in the one-particle Hamiltonian $H_0 = \frac{p^2}{2m} + V(\mathbf{r}) - \mu$ with the chemical potential μ , where we set the trapping frequencies to $f_x = f_y =: f_{\perp} \gg f_{\parallel} := f_z$, i.e., a cigar-shaped trap. In the following, we will show how to diagonalize Eq. (1) and thus obtain its eigenstates and energies which describe the single-particle excitations of the BCS condensate.

A. The BdG ground state

To calculate the ground-state properties of the BCS condensate it is instructive to write the eigenvalue equation corresponding to Eq. (1) as the BdG equation [36]

$$\begin{pmatrix} H_0 & \Delta(\mathbf{r}) \\ \Delta^*(\mathbf{r}) & -H_0^* \end{pmatrix} \begin{pmatrix} u_M(\mathbf{r}) \\ v_M(\mathbf{r}) \end{pmatrix} = E_M \begin{pmatrix} u_M(\mathbf{r}) \\ v_M(\mathbf{r}) \end{pmatrix}. \quad (3)$$

This equation has the form of a one-particle Schrödinger equation¹, which implies that H_{BdG} describes non-interacting quasiparticles, i.e., the single-particle excitations of the BCS condensate. Therefore, Eq. (3) can

¹ To be precise, the many-body nature of the BCS pairing is included in Eq. (3) via the self-consistent calculation of the BCS gap $\Delta(\mathbf{r})$ (see below).

be diagonalized which yields the corresponding single-particle wave functions $[u_M(\mathbf{r}), v_M(\mathbf{r})]$ and energies E_M . However, before we do so, we want to state that the single-particle states divide into two branches (one of positive energies $E_M = E_{m\alpha} > 0$ and one of negative energies $E_M = E_{m\beta} = -E_{m\alpha}$) that can be expressed by one another [37]. Accordingly, we simplify our formalism by writing the corresponding expressions –whenever possible– solely in terms of the positive-energy states and by dropping the index α . I.e., in the following we set $[u_m(\mathbf{r}), v_m(\mathbf{r})] := [u_{m\alpha}(\mathbf{r}), v_{m\alpha}(\mathbf{r})]$ and $E_m := E_{m\alpha}$. Furthermore, we transform into the excitation picture, i.e., we flip the β -branch $[(m\beta) \rightarrow (mb)]$ and leave the α -branch unchanged $[(m\alpha) = (ma)]$. This yields one twofold degenerate branch with $E_m = E_{ma} = E_{mb}$. The corresponding creation operators read

$$\gamma_{ma}^\dagger = \int [u_m(\mathbf{r})\Psi_\uparrow^\dagger(\mathbf{r}) + v_m(\mathbf{r})\Psi_\downarrow(\mathbf{r})] d^3r \quad (4)$$

$$\gamma_{mb}^\dagger = \int [u_m(\mathbf{r})\Psi_\downarrow^\dagger(\mathbf{r}) - v_m(\mathbf{r})\Psi_\uparrow(\mathbf{r})] d^3r. \quad (5)$$

We solve the BdG equation by expressing the single-particle states $[u_M(\mathbf{r}), v_M(\mathbf{r})]$ in terms of the bare atomic states, i.e., the eigenstates of the harmonic trap $\phi_i(\mathbf{r})$,

$$u_M(\mathbf{r}) = \sum_{i=1}^N u_M^{(i)} \phi_i(\mathbf{r}) \quad (6)$$

$$v_M(\mathbf{r}) = \sum_{i=1}^N v_M^{(i)} \phi_i(\mathbf{r}), \quad (7)$$

with $M \in \{ma, mb\}$. Here, we restrict the sum to atomic states from a window of width $\Delta\epsilon \sim 1\mu$ around the chemical potential (i.e., $0.5\mu < \epsilon < 1.5\mu$) to reduce the numerical effort².

Inserting this in the BdG equation, multiplying by $\phi_m(\mathbf{r})$ and integrating over \mathbf{r} yields:

$$\begin{pmatrix} \epsilon_1 - \mu & 0 & \cdots & 0 & (\Delta)_{11} & \cdots & (\Delta)_{1N} & \cdots \\ 0 & \epsilon_2 - \mu & \ddots & \vdots & \vdots & \ddots & \vdots & \cdots \\ \vdots & \ddots & \ddots & 0 & \vdots & \ddots & \vdots & \cdots \\ 0 & \cdots & 0 & \epsilon_N - \mu & (\Delta)_{N1} & \cdots & (\Delta)_{NN} & \cdots \\ (\Delta)_{11}^* & \cdots & \cdots & (\Delta)_{1N}^* & -\epsilon_1 + \mu & 0 & \cdots & 0 \\ \vdots & \ddots & \vdots & \vdots & 0 & -\epsilon_2 + \mu & \ddots & \vdots \\ \vdots & \ddots & \vdots & \vdots & \vdots & \ddots & \ddots & 0 \\ (\Delta)_{N1}^* & \cdots & \cdots & (\Delta)_{NN}^* & 0 & \cdots & 0 & -\epsilon_N + \mu \end{pmatrix} \begin{pmatrix} u_M^{(1)} \\ u_M^{(2)} \\ \vdots \\ u_M^{(N)} \\ v_M^{(1)} \\ v_M^{(2)} \\ \vdots \\ v_M^{(N)} \end{pmatrix} = E_M \begin{pmatrix} u_M^{(1)} \\ u_M^{(2)} \\ \vdots \\ u_M^{(N)} \\ v_M^{(1)} \\ v_M^{(2)} \\ \vdots \\ v_M^{(N)} \end{pmatrix}, \quad (8)$$

with $(\Delta)_{mn} := \int d^3r \phi_m^*(\mathbf{r}) \Delta(\mathbf{r}) \phi_n(\mathbf{r})$.³ However, the BCS gap can be expressed in terms of the Bogoliubov transformation [Eqs. (4) and (5)] which yields

$$\begin{aligned} \Delta(\mathbf{r}) = & -g \sum_{m,n} v_m^*(\mathbf{r}) u_n(\mathbf{r}) \langle \gamma_{ma}^\dagger \gamma_{na} \rangle \\ & + u_m(\mathbf{r}) u_n(\mathbf{r}) \langle \gamma_{mb} \gamma_{na} \rangle \\ & - v_m^*(\mathbf{r}) v_n^*(\mathbf{r}) \langle \gamma_{ma}^\dagger \gamma_{nb}^\dagger \rangle \\ & + u_m(\mathbf{r}) v_n^*(\mathbf{r}) \left[\langle \gamma_{nb}^\dagger \gamma_{mb} \rangle - \delta_{mn} \right], \quad (9) \end{aligned}$$

and for the ground-state gap

$$\Delta_{\text{GS}}(\mathbf{r}) = g \sum_m u_m(\mathbf{r}) v_m^*(\mathbf{r}). \quad (10)$$

Therefore, a diagonalization of Eq. (8) requires a self-consistent treatment together with Eq. (10). In doing so, we set the chemical potential $\mu = E_F$ with E_F the Fermi energy of the bare atomic system, i.e., we assume that the chemical potential is not effected by the BCS pairing. Strictly speaking this assumption is only valid in the deep BCS regime. However, our numerical data on the basis of the Anderson approximation (see section II C) show that it has no qualitative effect on the features studied in this work.

A final remark to Eq. (10): In the presented form the gap equation exhibits an ultraviolet-divergence, i.e., –strictly speaking– Eq. (10) needs to be regularized to ensure the convergence of the sum over the BdG eigenstates [2]. However, in our case we restrict those sums to a rather narrow energy range around the Fermi level (see above) and this numerical cutoff remedies the need for a further regularization. This will be different in the calculations based on the Anderson approximation, as will be discussed below.

² We have checked that the qualitative features investigated in this work are independent from the size of this window. However, the features shift quantitatively, e.g., the gaps and frequencies shift to larger values when increasing the window size.

³ To calculate matrix elements of the form $\int d^3r \phi_m(\mathbf{r}) \phi_n(\mathbf{r}) \phi_k(\mathbf{r}) \phi_l(\mathbf{r})$ we used an analytical expression derived in [38].

B. Quench dynamics

To calculate the dynamics of the BCS condensate we make use of the Bogoliubov transformation Eqs. (4) and (5). The quasiparticles resulting from that transformation are the single-particle excitations of the BCS phase, which are created, when the system is perturbed. All dynamical quantities investigated in the context of this work can be expressed in terms of expectation values of these quasiparticles. Therefore, we use Heisenberg's equation of motion for the quasiparticle operators to numerically calculate the dynamics of the quasiparticle expectation values.

To this end, we express the BdG Hamiltonian in terms of the single-particle operators for a general nonequilibrium situation where $\Delta(\mathbf{r}, t) \neq \Delta_{\text{GS}}(\mathbf{r})$, i.e., where the current value of the gap differs from the ground-state value $\Delta_{\text{GS}}(\mathbf{r})$. Thus, inserting Eqs. (4) and (5) into Eq. (1) where $\Delta = \Delta(\mathbf{r}, t) \neq \Delta_{\text{GS}}(\mathbf{r})$ and identifying Δ_{GS} via Eq. (10) yields

$$\begin{aligned} H_{\text{BdG}} &= \sum_m E_{ma} \left(\gamma_{ma}^\dagger \gamma_{ma} + \gamma_{mb}^\dagger \gamma_{mb} - 1 \right) \\ &+ \sum_{m,n} \left[(\Delta - \Delta_{\text{GS}})_{u_m^* v_n} + (\Delta^* - \Delta_{\text{GS}}^*)_{v_m^* u_n} \right] \gamma_{ma}^\dagger \gamma_{na} \\ &+ \sum_{m,n} \left[(\Delta - \Delta_{\text{GS}})_{u_m^* u_n^*} - (\Delta^* - \Delta_{\text{GS}}^*)_{v_m^* v_n^*} \right] \gamma_{ma}^\dagger \gamma_{nb}^\dagger \end{aligned}$$

$$\begin{aligned} &- \sum_{m,n} \left[(\Delta - \Delta_{\text{GS}})_{v_m v_n} - (\Delta^* - \Delta_{\text{GS}}^*)_{u_m u_n} \right] \gamma_{mb} \gamma_{na} \\ &+ \sum_{m,n} \left[(\Delta - \Delta_{\text{GS}})_{v_m u_n^*} + (\Delta^* - \Delta_{\text{GS}}^*)_{u_m v_n^*} \right] \gamma_{mb}^\dagger \gamma_{nb} \\ &- \sum_{m,n} \left[(\Delta - \Delta_{\text{GS}})_{v_m u_n^*} + (\Delta^* - \Delta_{\text{GS}}^*)_{u_m v_n^*} \right], \quad (11) \end{aligned}$$

with

$$(\Delta - \Delta_{\text{GS}})_{u_m v_n} := \int d^3 r u_m^*(\mathbf{r}) [\Delta(\mathbf{r}, t) - \Delta_{\text{GS}}(\mathbf{r})] v_n(\mathbf{r}). \quad (12)$$

We insert this into Heisenberg's equation of motion

$$\frac{d}{dt} A_H = \frac{i}{\hbar} [H_H, A_H] + \left(\frac{\partial}{\partial t} A \right)_H, \quad (13)$$

where A_H is the corresponding operator in the Heisenberg picture and $\left(\frac{\partial}{\partial t} A \right)_H = 0$ for the quasiparticle operators since all our calculations are performed with fixed basis states $[u_m(\mathbf{r}), v_m(\mathbf{r})]$. For the required single-particle expectation values this yields the following equations of motion:

$$\begin{aligned} i\hbar \frac{d}{dt} \langle \gamma_{ma}^\dagger \gamma_{na} \rangle &= -(E_m - E_n) \langle \gamma_{ma}^\dagger \gamma_{na} \rangle + \sum_l \left(\right. \\ &- \left[(\Delta - \Delta_{\text{GS}})_{u_l^* v_m} + (\Delta^* - \Delta_{\text{GS}}^*)_{v_l^* u_m} \right] \langle \gamma_{la}^\dagger \gamma_{na} \rangle + \left[(\Delta - \Delta_{\text{GS}})_{u_n^* v_l} + (\Delta^* - \Delta_{\text{GS}}^*)_{v_n^* u_l} \right] \langle \gamma_{ma}^\dagger \gamma_{la} \rangle \\ &+ \left. \left[(\Delta - \Delta_{\text{GS}})_{u_n^* u_l^*} - (\Delta^* - \Delta_{\text{GS}}^*)_{v_n^* v_l^*} \right] \langle \gamma_{ma}^\dagger \gamma_{lb}^\dagger \rangle - \left[-(\Delta - \Delta_{\text{GS}})_{v_l v_m} + (\Delta^* - \Delta_{\text{GS}}^*)_{u_l u_m} \right] \langle \gamma_{lb} \gamma_{na} \rangle \right) \quad (14) \end{aligned}$$

$$\begin{aligned} i\hbar \frac{d}{dt} \langle \gamma_{mb}^\dagger \gamma_{nb} \rangle &= -(E_m - E_n) \langle \gamma_{mb}^\dagger \gamma_{nb} \rangle + \sum_l \left(\right. \\ &- \left[(\Delta - \Delta_{\text{GS}})_{u_l^* v_m} + (\Delta^* - \Delta_{\text{GS}}^*)_{v_l^* u_m} \right] \langle \gamma_{lb}^\dagger \gamma_{nb} \rangle + \left[(\Delta - \Delta_{\text{GS}})_{u_n^* v_l} + (\Delta^* - \Delta_{\text{GS}}^*)_{v_n^* u_l} \right] \langle \gamma_{mb}^\dagger \gamma_{lb} \rangle \\ &+ \left. \left[(\Delta - \Delta_{\text{GS}})_{u_n^* u_l^*} - (\Delta^* - \Delta_{\text{GS}}^*)_{v_n^* v_l^*} \right] \langle \gamma_{la}^\dagger \gamma_{mb}^\dagger \rangle - \left[-(\Delta - \Delta_{\text{GS}})_{v_l v_m} + (\Delta^* - \Delta_{\text{GS}}^*)_{u_l u_m} \right] \langle \gamma_{nb} \gamma_{la} \rangle \right) \quad (15) \end{aligned}$$

$$\begin{aligned} i\hbar \frac{d}{dt} \langle \gamma_{mb} \gamma_{na} \rangle &= -i\hbar \frac{d}{dt} \left(\langle \gamma_{na}^\dagger \gamma_{mb}^\dagger \rangle \right)^* = (E_m + E_n) \langle \gamma_{mb} \gamma_{na} \rangle + \sum_l \left(\right. \\ &\left[(\Delta - \Delta_{\text{GS}})_{u_n^* v_l} + (\Delta^* - \Delta_{\text{GS}}^*)_{v_n^* u_l} \right] \langle \gamma_{mb} \gamma_{la} \rangle + \left[(\Delta - \Delta_{\text{GS}})_{u_n^* u_l^*} - (\Delta^* - \Delta_{\text{GS}}^*)_{v_n^* v_l^*} \right] \left(\delta_{ml} - \langle \gamma_{lb}^\dagger \gamma_{mb} \rangle \right) \\ &- \left. \left[(\Delta - \Delta_{\text{GS}})_{u_l^* u_m^*} - (\Delta^* - \Delta_{\text{GS}}^*)_{v_l^* v_m^*} \right] \langle \gamma_{la}^\dagger \gamma_{na} \rangle + \left[-(\Delta - \Delta_{\text{GS}})_{v_l u_m^*} + (\Delta^* - \Delta_{\text{GS}}^*)_{u_l v_m^*} \right] \langle \gamma_{lb} \gamma_{na} \rangle \right). \quad (16) \end{aligned}$$

We solve these nonlinearly coupled equations of motion

for the initial value problem defined by an instantaneous

interaction quench. I.e., we start from the ground state corresponding to a scattering length a_i and instantaneously switch to a different value⁴ $a_i \rightarrow a_f$. Therefore, during the quench at the time $t = 0$ the system has no time to relax to the new ground state corresponding to a_f but it remains in the old ground state corresponding to a_i . I.e., all quasiparticle expectation values of the form $\langle \gamma_M^\dagger \gamma_{M'} \rangle$ and $\langle \gamma_M \gamma_{M'} \rangle$ with $M \in \{ma, mb\}$ and $M' \in \{m'a, m'b\}$ which correspond to the old ground state vanish for $t = 0$. With this in mind, we invert the Bogoliubov transformation for the operators γ_M in the old basis before the quench and insert the resulting expressions for Ψ_σ and Ψ_σ^\dagger into the quasiparticle operators in the new basis after the quench [Eqs. (4) and (5)]. This yields the initial values for the dynamics

$$\begin{aligned} \langle \gamma_{ma}^\dagger \gamma_{na} \rangle|_{t=0} &= \sum_k \int d^3r \left[v_m(\mathbf{r}) \tilde{u}_k(\mathbf{r}) - u_m(\mathbf{r}) \tilde{v}_k(\mathbf{r}) \right] \\ &\cdot \int d^3r' \left[v_n^*(\mathbf{r}') \tilde{u}_k^*(\mathbf{r}') - u_n^*(\mathbf{r}') \tilde{v}_k^*(\mathbf{r}') \right] \end{aligned} \quad (17)$$

$$\begin{aligned} \langle \gamma_{ma}^\dagger \gamma_{nb}^\dagger \rangle|_{t=0} &= \sum_k \int d^3r \left[v_m(\mathbf{r}) \tilde{u}_k(\mathbf{r}) - u_m(\mathbf{r}) \tilde{v}_k(\mathbf{r}) \right] \\ &\cdot \int d^3r' \left[v_n(\mathbf{r}') \tilde{v}_k^*(\mathbf{r}') + u_n(\mathbf{r}') \tilde{u}_k^*(\mathbf{r}') \right] \end{aligned} \quad (18)$$

$$\langle \gamma_{mb} \gamma_{na} \rangle|_{t=0} = \left(\langle \gamma_{na}^\dagger \gamma_{mb}^\dagger \rangle|_{t=0} \right)^* \quad (19)$$

$$\begin{aligned} \langle \gamma_{mb}^\dagger \gamma_{nb} \rangle|_{t=0} &= - \sum_k \int d^3r \left[v_m^*(\mathbf{r}) \tilde{v}_k(\mathbf{r}) + u_m^*(\mathbf{r}) \tilde{u}_k(\mathbf{r}) \right] \\ &\cdot \int d^3r' \left[v_n(\mathbf{r}') \tilde{v}_k^*(\mathbf{r}') + u_n(\mathbf{r}') \tilde{u}_k^*(\mathbf{r}') \right] + \delta_{mn}, \end{aligned} \quad (20)$$

where \tilde{u}_m and \tilde{v}_m refer to the single-particle states before the quench and u_m and v_m to those after the quench.

With Eqs. (17)-(20) we can numerically integrate the equations of motion and thus calculate the gap dynamics for a gas of ^6Li in a 3D harmonic trap via Eq. (9). In section III A we will present the corresponding results for the phase dynamics of the gap. However, before that we introduce Anderson's approximation which we will use to perform elaborate parameter scans and to calculate the gap dynamics for systems with rather large particle number that are numerically too complex to address within the full BdG approach. In doing so, we will restrict our explanations to the main aspects of the approximation. A detailed description of the corresponding formalism with all expressions derived from the above can be found in our previous work [20].

C. Anderson's Approximation

In Anderson approximation the expansion of the quasiparticle wave function in Eqs. (6) and (7) is truncated such that $u_m(\mathbf{r}) = u_m \phi_m(\mathbf{r})$ and $v_m(\mathbf{r}) = v_m \phi_m(\mathbf{r})$. This strongly simplifies the formalism presented above. For the ground-state properties the diagonalization of Eq. (8) directly yields

$$E_m = \sqrt{(\varepsilon_m - \mu)^2 + (\Delta_{mm}^{\text{GS}})^2} \quad (21)$$

and

$$u_m = \sqrt{\frac{1}{2} \left(1 + \frac{\varepsilon_m - \mu}{E_m} \right)} \quad v_m = \sqrt{\frac{1}{2} \left(1 - \frac{\varepsilon_m - \mu}{E_m} \right)}. \quad (22)$$

which –in combination with Eq. (10)– leads to a BCS-like selfconsistency equation, that we solve numerically. In doing so, we use much larger energy windows in the sum over the states as compared to the full BdG approach since the numerical effort is strongly reduced in the case of the Anderson approximation. Thereby, we employ the regularization scheme introduced in [20]. Only when directly comparing the full BdG equations with the Anderson approximation (Sec. III A) we use the same cutoffs in both calculations to improve the comparability of the respective calculations.

For the dynamical situation we furthermore assume that $(\Delta - \Delta_{\text{GS}})_{x_m y_n} = (\Delta - \Delta_{\text{GS}})_{x_m y_n} \delta_{mn}$ with $x_m, y_m \in \{u_m, v_m\}$, i.e., that the main implications of the Anderson approximation $\Delta_{mn}^{\text{GS}} = \Delta_{mn}^{\text{GS}} \delta_{mn}$ holds for the dynamical situation as well. That leads to a great simplification of the equations of motion.

However, strictly speaking Anderson's approximation is only valid if $\Delta_{mn}^{\text{GS}} \ll \delta\varepsilon$ with $\delta\varepsilon$ the level spacing of the harmonic eigenenergies. In general, this only holds for weak coupling, i.e., deep in the BCS regime, and/or for strong confinements and thus large level spacing. Nevertheless, our numerical data show that the approximation reproduces all the main features investigated in this work even for moderate confinements in the BCS-BEC crossover regime (cf. section III A).

III. RESULTS

In the following, we investigate the phase dynamics of the spatially averaged BCS gap⁵

$$\bar{\Delta}(t) = \frac{1}{V} \int d^3r \Delta(\mathbf{r}, t) \quad (23)$$

for an ultracold gas of ^6Li in a cigar-shaped harmonic trap. We use $V = l_x l_y l_z$ with l_α being the oscillator

⁴ This assumption of an instantaneous quench is valid, since the experimentally achieved quench times \sim ns are way below the timescales of the gap dynamics \sim ms.

⁵ In our case the phase of the gap φ is nearly homogeneous (see below), i.e., $\bar{\varphi} \approx \varphi(\mathbf{r})$.

length in direction α as a normalization volume. We excite the system by interaction quenches $a_i \rightarrow a_f$.

In section III A we will identify the emergence of a Goldstone mode in the phase dynamics of the BCS gap with one dominant low-frequency contribution. Furthermore, we will show that the results obtained within the Anderson approximation are in good agreement with the full BdG solution. In section III B we will analyze this Goldstone mode over a wide range of parameters and we will show that its excitation spectrum is gapless and that its main frequency is not determined by the trap parameters but by the details of the excitation.

In section III C we will investigate the influence of the confinement parameters on the phase dynamics and by that the effect of the superfluid resonances found in [39]. Furthermore, in section III D we will evaluate the impact of the interaction quench-induced Goldstone mode on the single-particle excitations of the cloud which could provide an experimental access to the gapless phase mode.

A. Phase dynamics of the gap

Figure 2 shows the dynamics of the phase $\varphi = \arg(\bar{\Delta})$ of the spatially averaged BCS gap for a system with $f_{\perp} = 1$ kHz and $f_{\parallel} = 96$ Hz excited by quenches with the strength $\delta[1/(k_F a)] = 1/(k_F a_f) - 1/(k_F a_i) = -0.1$ at different positions in the BCS-BEC crossover. The particle number is set to $N_P = 120$ and the expansion of the single-particle wave functions in Eqs. (6) and (7) is restricted to atomic states from a window of width $\Delta\epsilon := 0.92E_F$ around the chemical potential (i.e., $\mu - 0.46E_F \leq \epsilon \leq \mu + 0.46E_F$). This is the limitation of our current numerical setup for the full BdG approach.

The solid lines in Fig. 2 show the data obtained by the full equations of motion (14) - (16). First of all, one clearly observes that –for all quenches– the phase dynamics of the gap is strongly dominated by a linear decrease in time. Therefore, after the quench the system performs a constant phase “motion” of the gap which nicely corresponds to the simplified picture of a Mexican-hat potential introduced in Fig. 1: The potential is flat inside the rim which implies a constant phase velocity, i.e., a steady oscillation inside the rim where the frequency of the latter –i.e., the frequency of the Goldstone mode– is defined by the time-averaged slope $f_G := \frac{1}{2\pi} \frac{\Delta\varphi}{\Delta t}$ where Δt is large compared to the intrinsic time scales of the system.⁶ The corresponding values are given by $f_G = 1.6$ Hz for the weakest coupling

⁶ We want to remark that the appearance of a Goldstone mode with a fixed frequency is similar to the case of the AC Josephson effect. There, a difference in the chemical potentials μ_i on the two sides of a Josephson junction leads to the emergence of a Goldstone mode with the frequency given by $f_G \sim (\mu_2 - \mu_1)$ [9]. In contrast, in our case the Goldstone mode is driven by the quench which drives the system instantaneously from an equilibrium into a non-equilibrium state.

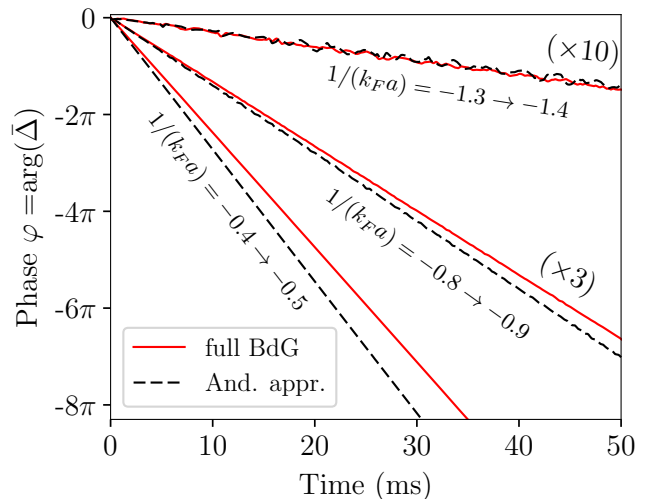


FIG. 2. (color online) Phase dynamics for the full BdG solution (solid lines) and the Anderson approximate solution (dashed lines) for $\delta[1/(k_F a)] = -0.1$ and different final coupling strengths: $1/(k_F a_f) = -0.5$, $1/(k_F a_f) = -0.9$ (scaled by a factor of 3) and $1/(k_F a_f) = -1.4$ (scaled by a factor of 10); parameters: $f_{\parallel} = 96$ Hz, $f_{\perp} = 1$ kHz, $N_P = 120$.

strength and $f_G = 21.9$ Hz for $1/(k_F a_f) = -0.9$ and $f_G = 118.7$ Hz for $1/(k_F a_f) = -0.5$ (for illustrative purposes the curves for the two weaker coupling strengths are scaled by a factor 3 and 10, respectively). Thus, the interaction quench-induced “phase velocity” strongly increases when approaching the unitary point $1/(k_F a) = 0$.

Furthermore, a closer look at Fig. 2 reveals that a higher-frequency oscillation exists on top of the linear contribution. This contribution is strongest for the system with $1/(k_F a_f) = -1.4$ and much weaker –and thus not directly visible in Fig. 2– for the stronger-coupling cases. A more detailed analysis shows that the corresponding frequencies again increase when approaching the unitary point, i.e., this dynamics is fast for large and slow for small coupling strengths. Nevertheless, the corresponding range of frequencies coincides with that from the spectrum of the Higgs mode. This indicates that the Higgs and the Goldstone mode are weakly coupled, where we observe that the influence of the Higgs mode increases when approaching the BCS limit $1/(k_F a) \ll -1$ and when increasing the modulus of quench strength $|\delta[1/(k_F a)]|$. However, the Higgs mode was extensively studied in [20]. Therefore, in this work we will not go into details about these contributions.

The dashed lines in Fig. 2 show the Anderson approximate solution corresponding to section II C (note that in order to improve the comparability here we have used an unregularized Anderson solution with the same cut-off as in the calculations without Anderson approximation). One can see that the approximate solution gives an overall good qualitative agreement with the full dynamics: It shows the same linear decrease in time with

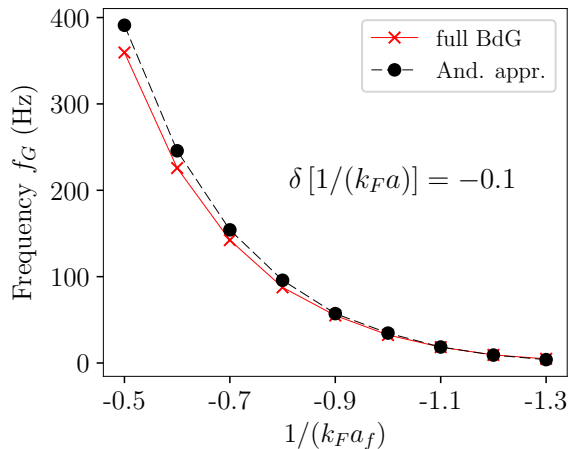


FIG. 3. (color online) Frequency of the Goldstone mode resulting from the full BdG solution (solid line) and from Anderson’s approximate solution (dashed line) for the same system as in Fig. 2 but varying $1/(k_F a_f)$ (to reduce the numerical effort we set $\Delta\epsilon = 0.58E_F$).

a –in the stronger coupling cases not directly visible– higher-frequency contribution on top. Again, the slow linear decrease corresponds to the Goldstone mode while the higher-frequency component results from the coupling to the Higgs mode⁷. However, one can observe as well that the quantitative deviations between the full and the approximate solution increase with increasing coupling strength: While –considering that the corresponding curves in Fig. 2 are scaled by a factor of 10– the frequency of the Goldstone mode, i.e., the slope of the linear contribution, matches very well for the case of $1/(k_F a_f) = -1.4$ the deviation of the two solutions becomes rather significant when increasing the coupling strength.

This is illustrated in Fig. 3. There, the frequencies of the Goldstone mode resulting from the full and from the approximate solution are shown for a fixed quench strength $\delta[1/(k_F a)] = -0.1$ and varying $1/(k_F a_f)$. One can clearly observe that the approximate solution reproduces well the qualitative trend, i.e., an overall increase of the frequency of the Goldstone mode when approaching the unitary point. Indeed, when entering the BCS regime even the quantitative values match very well. However, one can see as well, that the deviation between both solutions increases with increasing coupling strength and becomes rather large in the crossover regime. This indicates that Anderson’s approximation tends to break down –as expected– when approaching the unitary point.

Nevertheless, we want to emphasize that all features in the phase dynamics investigated in this work are fully reproduced by the Anderson approximation. Solely the shift in frequency between the full and the approximate solution increases with increasing coupling strength. Therefore, all following calculations of this work are performed in Anderson approximation which allows for a drastical reduction of computational effort and thus for a detailed investigation of parameter dependencies and of larger systems at all. In doing so, from now on all sums will be restricted to states from a window of size $2E_F$ around the Fermi level instead of $0.92E_F$ as before to ensure a better quantitative convergence of the obtained frequencies (cf. [20]).

Continuing in Anderson approximation we will now investigate the phase dynamics in closer detail, i.e., we will analyze the influence of the external parameters on the frequency f_G of the Goldstone mode and we will point out by which quantities it is determined. To do so, we will first investigate the influence of the coupling strength and of the details of the quench. In section III C we will focus on the effect of the confinement.

B. Influence of the quench

Figure 2 already suggests that the frequency of the Goldstone mode f_G depends on the details of the quench instead of being fixed by the external parameters of the cloud. The phase dynamics changes from a very slow decrease for the system in the BCS regime with $1/(k_F a_f) = -1.4$ to a rather fast decrease in the crossover regime with $1/(k_F a_f) = -0.5$. However, in Fig. 2 the quench strength by means of $\delta[1/(k_F a)]$ was kept fixed. Only the position in the BCS-BEC crossover was varied. Accordingly, we will in the following investigate the influence of the quench strength on the phase dynamics for one particular final coupling strength $1/(k_F a_f)$ in Fig. 4 and for a wider range of $1/(k_F a_f)$ in Fig. 5. In doing so, we will show, that the excitation spectrum of the interaction quench-induced Goldstone mode is gapless, i.e., it is a Goldstone mode in the original sense of the Goldstone theorem. Furthermore, we will show that its frequency can be adjusted by changing the details of the quench and that it is determined by the initial values of the dynamics and by the gap of the system after the quench.

Figure 4 shows the frequency of the Goldstone mode for a system with $1/(k_F a_f) = -0.9$ in the same trap as in Fig. 2 but –since we now apply Anderson’s approximation– for a larger particle number⁸ of $N_P = 1000$. The initial coupling strength $1/(k_F a_i)$ is varied,

⁷ The agreement of both solutions with respect to the Higgs mode may not look very convincing. However, already rather small deviations in the spectral composition of the Higgs mode result in large deviations in the time domain at larger times. I.e., the qualitative agreement of both solutions is in indeed good.

⁸ With our current numerical setup we can calculate the dynamics of single systems for up to $N_P \sim 10^4$ particles. However, there are no qualitative changes in the gap dynamics when increasing the particle number, i.e., here we restrict ourselves to rather small N_P to reduce the numerical effort.

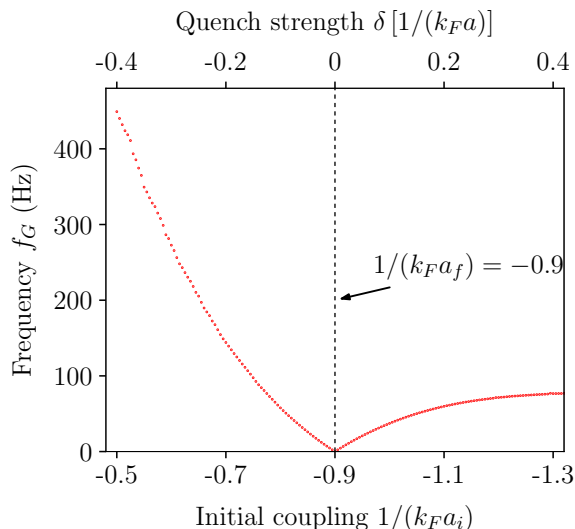


FIG. 4. (color online) Frequency of the Goldstone mode f_G for quenches with varying strength to $1/(k_F a_f) = -0.9$; parameters: $f_{\parallel} = 96$ Hz, $f_{\perp} = 1$ kHz, $N = 1000$.

i.e., the dependence of f_G on the quench strength is shown.

First of all, Fig. 4 demonstrates that the phase dynamics strongly depends on the quench strength: When approaching $1/(k_F a_i) = 1/(k_F a_f) = -0.9$, i.e., the point of quench strength $\delta [1/(k_F a)] = 0$, from either side [from larger or smaller values of $1/(k_F a_i)$] the frequency of the Goldstone mode continuously decreases to zero. Thus, the frequency of the Goldstone mode decreases with decreasing (modulus of the) quench strength and continuously vanishes for $\delta [1/(k_F a)] \rightarrow 0$. This implies that the excitation spectrum of the interaction quench-induced phase mode is indeed gapless as stated above.

Furthermore, we observe that the dependence of f_G on the quench strength in Fig. 4 is asymmetric: Negative quenches with $\delta [1/(k_F a)] < 0$, i.e., those on the left hand side of Fig. 4, lead to a stronger increase in f_G and thus to larger frequencies than positive quenches. This asymmetry is linked to the fact that the same excitation strength in terms of $1/(k_F a)$, i.e., the same $|\delta [1/(k_F a)]|$, results in different actual changes in the scattering length $|\delta a| = |a_f - a_i|$ depending on the position of the initial system in the crossover. Hence, negative quenches lead to much larger changes in the scattering length $|\delta a|$ – and therefore in the gap – than positive quenches. As we will show later on, this results in larger f_G . However, before we do so, we will demonstrate that the features found above hold for a wide range of quenches in the BCS-BEC crossover. Indeed, our numerical data indicate that the above found nature of the phase dynamics holds for all moderate quenches on the BCS side of the BCS-BEC crossover, i.e., for all quenches that can be associated with the phase II of the quantum quench phase diagram introduced in [41]. For quenches exceeding this

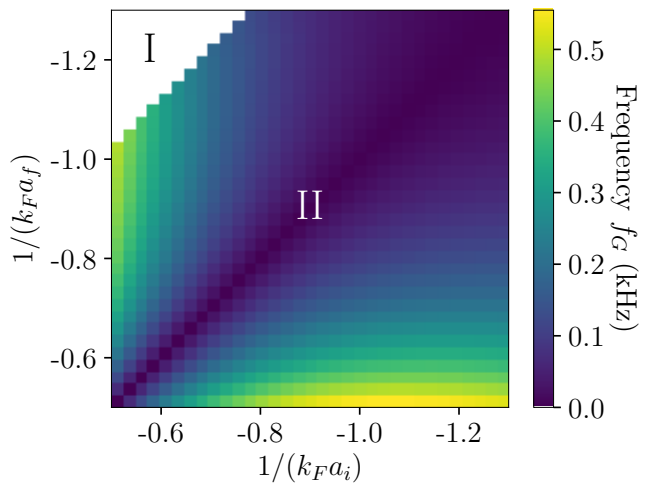


FIG. 5. (color online) Frequency of the Goldstone mode f_G for different excitations $1/(k_F a_i) \rightarrow 1/(k_F a_f)$ corresponding to phase II of the quantum quench phase diagram (see main text); quenches corresponding to phase I are not shown; parameters: $f_{\parallel} = 96$ Hz, $f_{\perp} = 1$ kHz, $N = 1000$.

range, the phase dynamics tends to become irregular. In particular, strong negative quenches which lead to a dynamical vanishing of the gap in the Higgs mode (phase I) exhibit a persistent but very irregular phase dynamics which makes the definition of a frequency of the Goldstone mode arbitrary. However, in this work we restrict ourselves to the investigation of the regular phase dynamics in the gapless Goldstone mode, i.e., to quenches in the phase II.

To this end, Fig. 5 shows the dependence of f_G on the quench strength for varying $1/(k_F a_f)$, i.e., each horizontal line in Fig. 5 corresponds to a plot like in Fig. 4 but for a different coupling strength.

Indeed, one observes on the basis of Fig. 5 that the nature of the Goldstone mode described above holds for all phase II quenches investigated here (we omit the quenches in the upper left corner corresponding to phase I). For each horizontal line in Fig. 5 we see a decrease of f_G with decreasing modulus of the quench strength $|\delta [1/(k_F a)]|$ as found above with a continuously vanishing Goldstone mode when approaching $1/(k_F a_i) = 1/(k_F a_f)$. However, furthermore one can see, that the frequency of the Goldstone mode also depends on the vertical position of the quench in Fig. 5: It is largest for quenches at the bottom, i.e., for systems with large coupling strength. In fact, one can observe that quenches with the same $|\delta [1/(k_F a)]|$ but opposite directions, e.g., those corresponding to the points $[1/(k_F a_i), 1/(k_F a_f)] = (-1.0, -0.5)$ and $[1/(k_F a_i), 1/(k_F a_f)] = (-0.5, -1.0)$ lead to significantly different f_G . This indicates that f_G depends not only on the quench strength but also on the coupling strength of the system after the quench, i.e., a stronger coupling results in a larger f_G . In the following, we will explain both these features – the dependence

on the quench strength and the dependence on the final coupling strength— by taking into account that the only parameters of the dynamics affected by the quench are the initial values of the excitation and the gap after the quench. We will isolate the effects of both quantities on the basis of Fig. 5 and Eqs. (17)-(20).

To do so, we at first want to state that the frequency of the Goldstone mode depends linearly on the initial values of the dynamics which in Anderson approximation read (cf. [20] and Eqs. (17)-(20))

$$\begin{aligned} \left\langle \gamma_{ma}^\dagger \gamma_{ma} \right\rangle \Big|_{t=0} &= (v_m \tilde{u}_m - u_m \tilde{v}_m)^2 =: x_m^{(0)} \\ \left\langle \gamma_{ma}^\dagger \gamma_{mb}^\dagger \right\rangle \Big|_{t=0} &= (v_m \tilde{u}_m - u_m \tilde{v}_m) (v_m \tilde{v}_m + u_m \tilde{u}_m) \\ &=: y_m^{(0)}, \end{aligned} \quad (24)$$

with \tilde{u}_m and \tilde{v}_m (u_m and v_m) being the Anderson amplitudes before (after) the quench [see Eq. (22)]. Indeed, our numerical data show that by artificially multiplying these initial values by a factor k the frequency f_G increases by the same factor⁹, i.e.,

$$f_G \left(k \cdot \{x_m^{(0)}, y_m^{(0)}\} \right) = k f_G \left(\{x_m^{(0)}, y_m^{(0)}\} \right).$$

This means that –whatever the actual system parameters (a_f , N_P , f_{\parallel} , f_{\perp}) are– the frequency of the Goldstone mode can be tuned by adjusting the initial values of the dynamics. As Eqs. (22) and (24) imply, the latter depend on the gaps of the system before and after the quench which are defined by the quench.

A detailed evaluation of Eqs. (24) shows that the initial values are large when the difference between the gaps before and after the quench and thus between the amplitudes (\tilde{u}_m, \tilde{v}_m) and (u_m, v_m) is large. This is the case for strong quenches, i.e., strong quenches result in large initial values which well coincides with the above findings for f_G . However, Eqs. (24) also show that the amplitude of the initial excitation is independent from the quench direction. When changing the quench direction, i.e., when interchanging (\tilde{u}_m, \tilde{v}_m) \Leftrightarrow (u_m, v_m) in Eqs. (24), only the sign of the anomalous initial values $\left\langle \gamma_{ma}^\dagger \gamma_{mb}^\dagger \right\rangle \Big|_{t=0}$ changes. Therefore, the initial values for quenches with the same $|\delta [1/(k_F a_f)]|$ but opposite directions have the same strength but –as observed above– the frequency is larger for the respective positive quench to the stronger coupling $1/(k_F a_f)$. This indicates that the frequency of the Goldstone mode also depends on the actual coupling strength of the system after the quench.

We can conclude the results of this paragraph: The excitation spectrum of the Goldstone mode of the BCS gap of a 3D confined ultracold Fermi gas excited by an

interaction quench is gapless and the frequency of the Goldstone mode can be tuned in a wide range by adjusting the strength of the quench. Again, this coincides with the simplified picture of Fig. 1: However small the quench-induced initial “momentum” of the phase dynamics might be, it results in a constant “phase motion” inside the rim. This is –in simple words– the consequence of the Goldstone theorem, which therefore can well be observed in the dynamics after an interaction quench.

However, the fact that in our case the Goldstone mode is gapless and that its frequency can be adjusted by the strength of the excitation stands in contrast to the experimental and theoretical findings of Refs. [21–34]. There, the frequency of the phase dynamics was found to be fixed by the frequencies of the trapping potential. Nevertheless, this discrepancy can be explained by the circumstance that in the previous works the dynamics was induced by spatially inhomogeneous perturbations of the cloud, e.g., by confinement quenches or optical excitations. Such a spatial perturbation creates a motion of the superfluid in the trap with a time-dependent velocity v_s . This directly induces a dynamics of the phase of the gap via [1]

$$\mathbf{v}_s = \frac{\hbar}{2m} \nabla \arg[\Delta(\mathbf{r}, t)]. \quad (25)$$

On the one hand, this means that –whenever a superfluid velocity v_s is excited– the real-space dynamics is directly linked to a dynamics in the Goldstone mode. In this sense, the latter can be observed through the motion of the cloud. On the other hand, the trapping potential governs the real-space dynamics of the cloud. Therefore, a direct coupling of the Goldstone mode to the real-space dynamics implies that the trap imprints its frequencies on the Goldstone mode. For inhomogeneous excitations f_G is thus pushed to the trap frequencies as found in the previous works.¹⁰

In our case the excitation is spatially homogeneous and does not –as our numerical data confirm– produce any significant phase gradients. Therefore, no real-space dynamics of the cloud is induced by the interaction quench which implies that the phase dynamics does not couple to the trap. Accordingly, the excitation spectrum of this *homogeneous* Goldstone mode remains gapless. In this sense the interaction quench-induced Goldstone mode remains pure.

C. Impact of the superfluid resonances

In this section we want to study the influence of the confinement on the frequency of the gapless Goldstone

⁹ For the situation of strong interactions and strong quenches even an analytical expression can be found: $\omega_G = 2\pi f_G \approx \text{Im}(\frac{d}{dt}\bar{\Delta})|_{t=0}/\bar{\Delta}_{\text{GS}}$.

¹⁰ Actually, both manifestations of the Goldstone mode –the gapped inhomogeneous and the gapless one– may exist at the same time depending on the nature of the excitation.

mode and by that the impact of the size-dependent superfluid resonances theoretically predicted in [39]. To do so, we will investigate the dependence of the phase dynamics on the trapping frequency in x-y direction f_{\perp} for a system with fixed $f_{\parallel} = 96$ Hz, $N_P = 1000$ atoms in the trap and a quench given by $1/(k_F a) = -0.8 \rightarrow -0.9$. The complementary situation, i.e., a fixed f_{\perp} with varying f_{\parallel} produces the same effects. Therefore, the influence of f_{\parallel} will not be investigated separately.

Figure 6 shows the frequency of the gapless Goldstone mode for the above system over a wide range of f_{\perp} . One can see, that –on top of a global increasing trend¹¹– f_G exhibits a series of local maxima for different values of f_{\perp} . The distance of the maxima increases with increasing f_{\perp} while at the same time the maxima become more pronounced. I.e., the maxima in f_G occur less frequent but more pronounced when approaching higher values of f_{\perp} .

Furthermore, the dashed lines in Fig. 6 indicate the positions of integer system parameter $S = \mu/\hbar\omega_{\perp}$ with $\omega_{\perp} = 2\pi f_{\perp}$. These positions indicate trap parameters where the minimum of an atomic subband crosses the chemical potential (for a detailed description of the band structure see section III D). To be precise: The distance between two atomic subbands is $\hbar\omega_{\perp}$ and the minimum of the lowest subband is at $\varepsilon = \hbar\omega_{\perp}$. Therefore, the integer part of S is the number of subbands that have a minimum below/at the chemical potential, i.e., the number of subbands crossing the chemical potential. One can see that every resonance closely follows such a point of integer system parameter S .

An explanation for this behavior can be given on the basis of the atypical BCS-BEC crossover [39]: On the one hand, the atomic states closest to the chemical potential contribute strongest to the pairing. On the other hand, the states with the lowest quantum numbers m_z which are located at the subband minima exhibit the strongest interaction matrix elements [20]. Therefore, each time an atomic subband crosses the chemical potential ($S = 1, 2, 3, \dots$) the pairing is enhanced and the system is shifted towards the unitary point. Following section II B, this results in a larger frequency of the gapless Goldstone mode.

However, the decrease of the impact of the resonances for increasing system parameter reflects the circumstance that for large S several subbands contribute to the pairing while only a small fraction of the corresponding atomic states exhibits an enhanced coupling due to the resonance. Thus, for increasing S the influence of the resonant states on the overall coupling decreases.

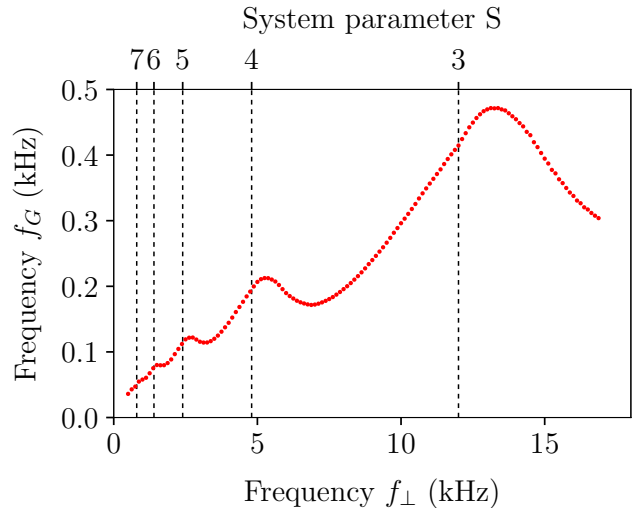


FIG. 6. (color online) Frequency of the gapless Goldstone mode f_G for fixed $f_{\parallel} = 96$ Hz, $N_P = 1000$ and $1/(k_F a) = -0.8 \rightarrow -0.9$; upper label: system parameter $S = \mu/\hbar\omega_{\perp}$.

D. Goldstone mode in the single-particle excitations

In this section we study the impact of the phase dynamics of the BCS gap on an experimentally more relevant physical quantity, the single-particle excitations of the condensate. An experimental investigation of the single-particle excitations has already been reported in [42] via RF-spectroscopy. Thus, they could provide a convenient access to the quench dynamics investigated here. Indeed, we will show that the gapless Goldstone mode is directly visible in the dynamics of the single-particle occupations and that it leads to a full inversion of the lowest-lying single-particle states. We will demonstrate this by investigating the effect of the phase dynamics on individual occupations as well as on the whole single-particle band structure.

In doing so, we focus on a cloud with the confinement frequencies given by $f_{\parallel} = 56$ Hz and $f_{\perp} = 4$ kHz, with $N_P = 1700$ atoms in the trap and with an excitation of $1/(k_F a) = -0.8 \rightarrow -0.9$. For such a cigar-shaped trap the atomic energies $\varepsilon_{m_x, m_y, m_z} := \varepsilon_m$ are strongly separated with respect to m_x and m_y and comparatively dense with respect to m_z , i.e., they form subbands. The single-particle energies of Eq. (21) inherit this band structure which can be seen in Fig. 7.

There, a plot of the single-particle energies against the quantum number m_z is shown for the system introduced above. One clearly observes several subbands each of which corresponds to certain sets of quantum numbers (m_x, m_y) , where –due to the cylindrical symmetry of the system– each subband is $2(m_x + m_y + 1)$ fold degenerate (the factor 2 results from the degeneracy of the two single-particle branches corresponding to the two spin

¹¹ This global increase is due to the circumstance that the density of the condensate and thus the gap increases when f_{\perp} is increased with fixed f_{\parallel} and N_P .

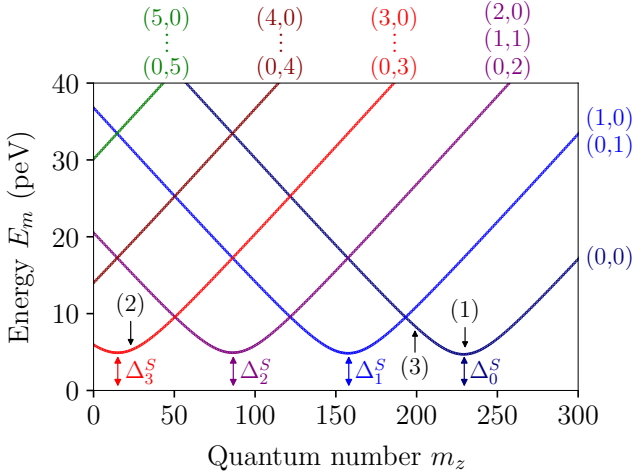


FIG. 7. (color online) Single-particle energies for a strongly confined Fermi gas in a BCS phase with four atomic subbands crossing the chemical potential; Δ_i^S denotes the gap of the subbands with $m_x + m_y = i$ and (m_x, m_y) denotes the subband index (see main text); the marked states (1), (2), (3) are discussed below; parameters: $f_{\parallel} = 56$ Hz, $f_{\perp} = 4$ kHz, $N = 1700$ and $1/(k_F a) = -0.9$.

configurations)¹². Furthermore, the four subbands with the lowest sets of quantum numbers (m_x, m_y) show minima when the corresponding atomic subbands cross the chemical potential, i.e., at different values for m_z . The states located at the minima thus lie in close vicinity to the chemical potential and contribute strongly to the BCS pairing (the expectation values $\Delta_{m_m}^{\text{GS}}$ corresponding to these states, i.e., the subband gaps, will be denoted as Δ_i^S with $i = m_x + m_y$ being the subband index; see Fig. 7). The higher atomic subbands with $m_x + m_y \geq 4$ do not cross the chemical potential. The corresponding single-particle subbands therefore do not exhibit any minima.

Since the single-particle operators corresponding to the energies of Fig. 7 –i.e., those of Eqs. (4) and (5)– are defined in the excitation picture all energy states of Fig. 7 are not occupied in the ground state before the quench. But, during the temporal evolution following the quench occupations of the order of 1 are created. We will show this explicitly for three particular single-particle states [marked as (1), (2) and (3) in Fig. 7], one close to the minimum of the subband (1,2) ($E_m = 5.2$ peV), one at the minimum of the subband

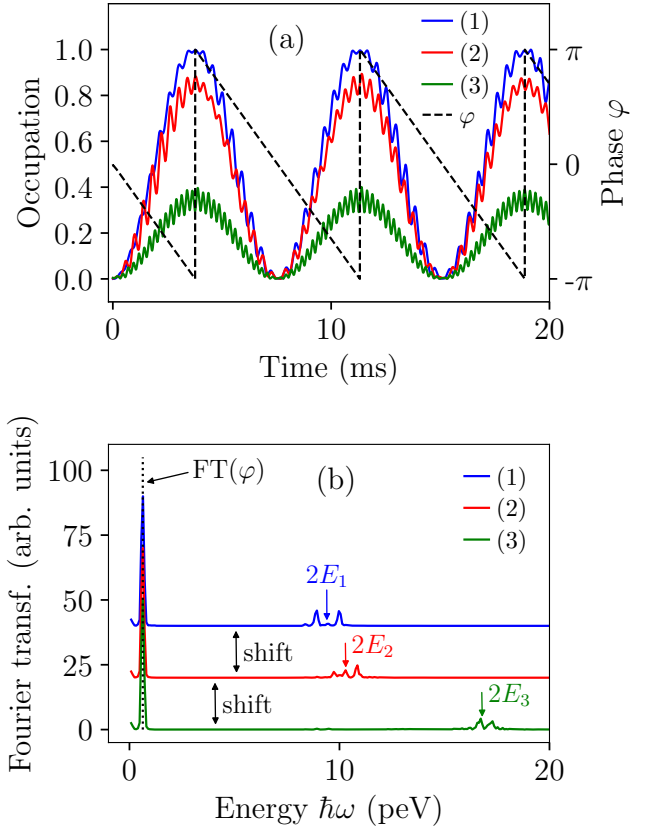


FIG. 8. (color online) (a) Dynamics of three particular single-particle occupations, one state of higher energy (3) and two from subband minima (1), (2) (see Fig. 7). (b) Fourier transform of the functions in (a).

(0,0) ($E_m = 4.7$ peV) and one at a higher energy in the subband (0,0) ($E_m = 8.4$ peV). Furthermore, we will identify the gapless Goldstone mode of the BCS gap in the corresponding dynamics.

The dynamics of the three single-particle occupations is shown in Fig. 8 (a) for the first 20 ms after the quench. We clearly observe that all occupations oscillate in phase with one dominant low frequency. The states (1) (blue line) and (2) (red line) have a large amplitude of the order of 1 while the amplitude of state (3) (green line) is much smaller. Furthermore, the three occupations each exhibit an individual weak higher-frequency component which has the largest frequency for the state (3) of high energy. However, we find that the amplitude of the higher-frequency component increases with decreasing the scattering length, i.e., when entering the BCS regime with $1/(k_F a) < -1$.

A comparison of the single-particle dynamics with the dynamics of the phase of the gap [Fig. 8 (a); dashed line] shows that the dominant low oscillation frequency originates from the Goldstone mode of the gap: The phase of the gap shows the same linear dynamics as in section II B with a rate corresponding to the low-frequency part of the

¹² Actually, subbands with different and not just interchanged quantum numbers (m_x, m_y) are not exactly degenerate due to slightly different subband gaps Δ_m^S (on the order of 0.1 peV for the investigated systems). For example: The subbands (0,3) and (3,0) are exactly degenerate, whereas the subbands (0,3) and (1,2) are split by ~ 0.5 peV. However, in the presented plots and with the assumed experimental accuracy this splitting is not resolved.

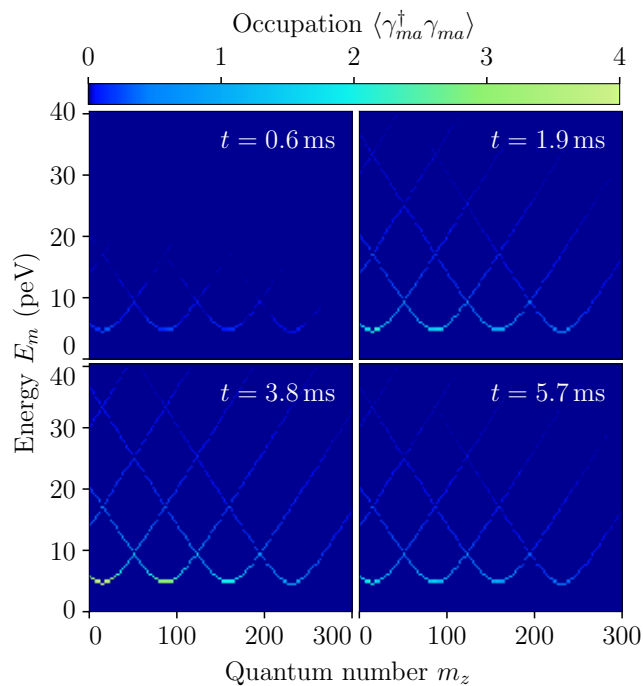


FIG. 9. (color online) Single-particle occupations at different times after the interaction quench; parameters: See Fig. 7.

single-particle occupations. Thus, the gapless Goldstone mode is directly visible in the excitation dynamics of the condensate.

To investigate the single-particle dynamics in closer detail, Figure 8 (b) shows the Fourier spectrum of the data of Fig. 8 (a). Again, we observe that the dominant low frequencies of the occupations and the phase of the BCS gap exactly match. But, the origin of the higher frequencies in the excitation dynamics can now be seen as well: Besides the dominant low-frequency components each spectrum exhibits a series of weak peaks at approximately twice the energy of the corresponding single-particle state. I.e., the higher-frequency components result from an eigenoscillation of the single-particle occupations. In Ref. [20] a sum of all eigenoscillations was shown to result in the Higgs mode of the gap. The higher-frequency components can thus be understood as fragments of the Higgs mode of the BCS gap.

At last, –to analyze the impact of the gapless Goldstone mode on the whole single-particle spectrum– Figure 9 shows snapshots of the single-particle occupations plotted against the quantum number m_z and the excitation energy E_m , like they could be measured by angle- and momentum-resolved RF spectroscopy [42], for a series of time steps after the quench. The first snapshot corresponds to the time $t = 0.6$ ms and thus directly follows the quench. Here, the excitations are rather weak and can hardly be seen. However, going on in time we observe that all occupations increase in phase until the time $t = 3.8$ ms, where the maximum occupation of all

states is reached. Afterwards the occupations decrease until the initial situation is reached again. Thus, Fig. 9 is an illustration of the in-phase oscillation of all single-particle occupations due to the gapless Goldstone mode.

In addition, –neglecting the contributions from the eigenoscillation– the snapshot for $t = 3.8$ ms provides a map of the amplitude of the single-particle oscillations since here the dominant low-frequency part of all occupations exhibits its maximum value. On the basis of this amplitude map one observes, that the amplitude distribution shows a resonance behaviour: The amplitude is largest for states with low quantum number m_z and low energy E_m and decreases with increasing values of m_z and E_m . In fact, directly at the minimum of the subbands with $m_x + m_y = 3$ the oscillation amplitude is 4, decreasing by 1 for every next lower subband $m_x + m_y$. However, this dependence is due to the $(m_x + m_y + 1)$ -fold degeneracy of the subbands (only the particle-like excitations of the single-particle branch a are shown). I.e., the oscillation amplitude of each individual single-particle occupation at a subband minimum is 1. Thus, the single-particle occupations at the subband minima exhibit a full inversion.

Concluding this section we can thus state: We have shown that the gapless Goldstone mode of an interaction-quenched ultracold Fermi gas directly couples to the single-particle occupations and leads to a full inversion of the lowest-lying states. An experimental access to the dynamical single-particle occupations would thus allow for a direct observation of the massless Goldstone Boson predicted by the Goldstone theorem. However, we want to remark that an application of RF-spectroscopy –a state-of-the-art experimental access to the single-particle excitations [42, 43]– to the dynamical situation is restricted to the observation of the inhomogeneous phase dynamics. It turns out that it does not contain any signature of the gapless homogeneous Goldstone mode (see appendix). Therefore, at least a modification of this experimental technique would be required to observe the gapless Goldstone mode via the single-particle excitations.

IV. CONCLUSION

In conclusion, we have calculated the dynamics of a confined ultracold ${}^6\text{Li}$ gas at $T = 0$ induced by an interaction quench on the BCS side of the BCS-BEC crossover. We used a full dynamical BdG approach to set up and solve the equations of motion for the single-particle occupations and coherences. In doing so, we have shown that the interaction quench excites a low-energy linear dynamics of the complex phase of the BCS gap, i.e., a Goldstone mode. We have analyzed this Goldstone mode over a wide range of parameters showing that its excitation spectrum is gapless and that its main frequency is not fixed by the trap frequencies but that it is determined by the details of the quench. Furthermore, we found that the atypical BCS-BEC crossover leads to resonances

in the gapless Goldstone mode. Finally, we investigated the impact of the gapless Goldstone mode on the single-particle occupations. We have shown that it leads to an in-phase oscillation of the whole single-particle spectrum with a full inversion of the lowest-lying single-particle states which could provide an experimental access to the gapless homogeneous Goldstone mode.

Appendix: Gapless Goldstone mode and RF spectroscopy

One way to study the single-particle occupations in experiment is RF spectroscopy as was shown in Ref. [42]. There, a first direct measurement of the single-particle excitations via RF spectroscopy was achieved for a thermal superfluid gas of ultracold ^{40}K in the BCS-BEC crossover. An application of RF spectroscopy to the dynamical situation could thus allow for a direct observation of the Goldstone mode without coupling it to the trap. This could be achieved, e.g., via a pump-probe like experimental setup: By introducing a delay time t between the quench (the ‘‘pump pulse’’) and the actual RF measurement (the ‘‘probe pulse’’) a time-resolved single-particle spectrum like in Fig. 9 could be obtained. However, in the following we will show that RF signals give a direct measurement of the single-particle occupations only if no single-particle coherences are present. In contrast, we will demonstrate that –for our case of a coherent evolution of the condensate– the single-particle coherences cancel the signature of the gapless Goldstone mode in the RF signal and thus prohibit its direct observation via RF spectroscopy.

The basic principle of RF spectroscopy applied to ultracold Fermi gases is to optically excite the atoms from one of the two hyperfine states of the condensate, i.e., the state denoted as $|k \uparrow\rangle$, to a third hyperfine state which is not involved in the BCS pairing (following Ref. [44] we will denote this state as $|k\sigma\rangle$ with $\sigma = 3$; depending on the atom species used the actual spin of the corresponding hyperfine state will be different though). Then, the resulting occupations of the third hyperfine state can be used –at least in the absence of coherences between the single-particle states– as a direct measure of the corresponding single-particle occupations (see below and [44]).

As stated above, an RF excitation results in a simultaneous spin flip of all atoms in the cloud which is described by the operator [44]

$$\hat{V} = V_0 \sum_k \left(c_{k3}^\dagger c_{k\uparrow} + c_{k\uparrow}^\dagger c_{k3} \right), \quad (\text{A.1})$$

with $c_{k\sigma}^\dagger$ ($c_{k\sigma}$) creating (annihilating) one atom in the state with quantum number k and spin index $\sigma \in \{\uparrow, \downarrow, 3\}$. Here, we assume the excitation to be orthogonal with respect to the quantum number k , i.e., we only consider transitions $|k \uparrow\rangle \rightarrow |k'3\rangle$ with $k = k'$. Strictly

speaking this applies only to very large systems where k corresponds to the wave number and if we furthermore assume $\hbar k_{RF} \ll \hbar k$, i.e., that the momentum of the photons is much smaller than the momentum of the atoms. However, in Anderson Approximation transitions with $k \neq k'$ do not contribute to the RF signal since all nondiagonal single-particle expectation values vanish (see below). Thus, we can apply Eq. (A.1) to our current situation.

Following [44], we use

$$c_{k\uparrow} = u_k \gamma_{ka}^\dagger - v_k \gamma_{kb} \quad (\text{A.2})$$

and we furthermore assume the third hyperfine state to be initially empty, i.e., $c_{k3}|\Psi(t)\rangle = 0$ with $|\Psi(t)\rangle$ the state of the condensate before the RF pulse. This yields:

$$\hat{V} = V_0 \sum_k c_{k3}^\dagger \left(u_k \gamma_{ka}^\dagger - v_k \gamma_{kb} \right). \quad (\text{A.3})$$

Therefore, the RF excitation transfers single atoms to the state $|k3\rangle$ by creating a quasiparticle in the single-particle state ka and destroying one in state kb . However, we are interested in the occupations of state $|k3\rangle$ after the excitation, i.e., we have to investigate the transitions governed by the matrix elements

$$M_k = \langle f|V|\Psi(t)\rangle, \quad (\text{A.4})$$

where $|\Psi(t)\rangle = |\gamma(t)\rangle|0\rangle_3$ is composed of the quasiparticle contribution $|\gamma(t)\rangle$ and the vacuum of the third hyperfine state $|0\rangle_3$. Since the exact quasiparticle configuration after the RF pulse is not relevant, the final state of the transition $|f\rangle$ needs to take into account all possible end states for the quasiparticles, i.e.,

$$|f\rangle = \sum_{k'} \left(u_{k'} \gamma_{k'a}^\dagger - v_{k'} \gamma_{k'b} \right) |\gamma(t)\rangle |k3\rangle. \quad (\text{A.5})$$

Inserting this into Eq. (A.4) and keeping in mind that in Anderson approximation $\langle \gamma_{ma}^\dagger \gamma_{na/b} \rangle = \langle \gamma_{ma}^\dagger \gamma_{nb} \rangle = 0$ for $m \neq n$ and that $\langle \gamma_{ma}^\dagger \gamma_{ma} \rangle = \langle \gamma_{mb}^\dagger \gamma_{mb} \rangle$ [20] we obtain

$$M_k \sim (u_k^2 - v_k^2) \langle \gamma_{ka}^\dagger \gamma_{ka} \rangle - 2u_k v_k \text{Re} \left(\langle \gamma_{ka}^\dagger \gamma_{kb} \rangle \right) + v_k^2. \quad (\text{A.6})$$

Therefore, the population in the state $|k3\rangle$ created by the RF pulse is a direct measure of the single-particle occupations if the single-particle coherences $\langle \gamma_{ka}^\dagger \gamma_{kb} \rangle$ vanish. This is the case for every thermal state of the condensate. I.e., –in that case– a momentum- and energy-resolved measurement of the occupation of the third hyperfine state maps the single-particle band structure (cf. [42]).

However, if single-particle coherences are present, they may interfere with the signal from the occupations and prohibit an observation of the latter. This is the case for our situation as can be seen by calculating M_k directly from Eq. (A.1) The quasiparticle part of the transition matrix elements M_k is basically given by the occupation of the atomic state $|k \uparrow\rangle$, i.e.,

$$M_k \sim \langle c_{k\uparrow}^\dagger c_{k\uparrow} \rangle \quad (\text{A.7})$$

Therefore, the overall transition matrix element considering all transitions to the third hyperfine state yields

$$M_{\text{total}} \sim \sum_k \langle c_{k\uparrow}^\dagger c_{k\uparrow} \rangle = N_{P\uparrow}. \quad (\text{A.8})$$

However, $N_{P\uparrow}$ is a conserved quantity during the free quench dynamics, i.e., during the dynamics before the RF pulse. Therefore, M_{total} and thus the overall RF-induced occupations of the third hyperfine state do not depend on the actual time of the RF measurement. This implies that the contribution from the Goldstone mode in the occupations has to be canceled out by a corresponding contribution in the single-particle coherences since all single-particle occupations oscillate in phase with respect to the gapless Goldstone mode. Therefore, every individual M_k is a constant with respect to the Goldstone mode. In that sense, particle conservation prohibits an observation of the gapless Goldstone mode via RF spectroscopy.

Indeed, our numerical data confirm that the contribution of the single-particle coherences to Eq. (A.6) exactly cancels out the signal of the Goldstone mode from the single-particle occupations. This confirms that the Goldstone mode in the present form is not visible via RF spectroscopy.

However, the same applies to the real-space dynamics of the condensate: For the same reasons as stated above

the gapless homogeneous Goldstone mode is not visible in the atomic density $\rho(\mathbf{r}, t)$ of the cloud. With Eqs. (4)-(5) one directly obtains

$$\begin{aligned} \rho(\mathbf{r}, t) &= \sum_\sigma \langle \hat{\Psi}_\sigma^\dagger(\mathbf{r}, t) \hat{\Psi}_\sigma(\mathbf{r}, t) \rangle \\ &= 2 \sum_k [(u_k^2 - v_k^2) \langle \gamma_{ka}^\dagger \gamma_{ka} \rangle \\ &\quad - 2u_k v_k \text{Re} \langle \gamma_{ka}^\dagger \gamma_{kb}^\dagger \rangle + v_k^2] |\varphi_k(\mathbf{r})|^2, \end{aligned} \quad (\text{A.9})$$

which has the same structure as Eq. (A.6). Therefore, the gapless homogeneous Goldstone mode does not couple to the real-space dynamics of the cloud as already stated in section II B. However, the resemblance of Eqs. (A.9) and (A.6) also implies that the Goldstone mode is visible in the RF signal for the case of inhomogeneous excitations. There, the symmetry between the single-particle excitations and coherences preventing the gapless homogeneous Goldstone mode from observation must be broken to allow for a collective oscillation of the cloud. Therefore, we state that in our case of a homogeneous excitation the Goldstone mode is visible neither in the single-particle excitations nor in the real-space dynamics of the cloud. But, for the same reason it must be visible in both quantities for the case of inhomogeneous excitations.

-
- [1] S. Giorgini, L. Pitaevskii, and S. Stringari, “Theory of ultracold atomic Fermi gases,” *Rev. Mod. Phys.* **80**, 1215–1274 (2008).
- [2] I. Bloch, J. Dalibard, and W. Zwerger, “Many-body physics with ultracold gases,” *Rev. Mod. Phys.* **80**, 885 (2008).
- [3] Steven Weinberg, *The quantum theory of fields*, Vol. 2 (Cambridge university press, 1996) pp. 332–352.
- [4] P. W. Higgs, “Broken symmetries and the masses of gauge bosons,” *Phys. Rev. Lett.* **13**, 508–509 (1964).
- [5] C. P. Burgess, “Goldstone and pseudo-Goldstone bosons in nuclear, particle and condensed-matter physics,” *Phys. Reports* **330**, 193–261 (2000).
- [6] D. Paulson, R. Johnson, and J. Wheatley, “Propagation of collisionless sound in normal and extraordinary phases of liquid ^3He below 3 mK,” *Phys. Rev. Lett.* **30**, 829 (1973).
- [7] D. Lawson, W. Gully, S. Goldstein, R. Richardson, and D. Lee, “Attenuation of zero sound and the low-temperature transitions in liquid ^3He ,” *Phys. Rev. Lett.* **30**, 541 (1973).
- [8] P. W. Anderson, “Random-phase approximation in the theory of superconductivity,” *Phys. Rev.* **112**, 1900 (1958).
- [9] David Pekker and CM Varma, “Amplitude/higgs modes in condensed matter physics,” *Annu. Rev. Condens. Matter Phys.* **6**, 269–297 (2015).
- [10] U. Bissbort, S. Götze, Y. Li, J. Heinze, J. S Krauser, M. Weinberg, C. Becker, K. Sengstock, and W. Hofstetter, “Detecting the amplitude mode of strongly interacting lattice bosons by Bragg scattering,” *Phys. Rev. Lett.* **106**, 205303 (2011).
- [11] M. Endres, T. Fukuhara, D. Pekker, M. Cheneau, P. Schauß, C. Gross, E. Demler, S. Kuhr, and I. Bloch, “The ‘Higgs’ amplitude mode at the two-dimensional superfluid/Mott insulator transition,” *Nature* **487**, 454–458 (2012).
- [12] R. Matsunaga, Y. I. Hamada, K. Makise, Y. Uzawa, H. Terai, Z. Wang, and R. Shimano, “Higgs amplitude mode in the BCS superconductors Nb $1-x$ Ti x n induced by terahertz pulse excitation,” *Phys. Rev. Lett.* **111**, 057002 (2013).
- [13] R. Matsunaga, N. Tsuji, H. Fujita, A. Sugioka, K. Makise, Y. Uzawa, H. Terai, Z. Wang, H. Aoki, and R. Shimano, “Light-induced collective pseudospin precession resonating with Higgs mode in a superconductor,” *Science* **345**, 1145–1149 (2014).
- [14] R.A. Barankov, L.S. Levitov, and B.Z. Spivak, “Collective Rabi oscillations and solitons in a time-dependent BCS pairing problem,” *Phys. Rev. Lett.* **93**, 160401 (2004).
- [15] R. A. Barankov and L. S. Levitov, “Synchronization in the BCS pairing dynamics as a critical phenomenon,” *Phys. Rev. Lett.* **96**, 230403 (2006).
- [16] E. A. Yuzbashyan, O. Tsyplatyev, and B. L. Altshuler, “Relaxation and persistent oscillations of the order parameter in fermionic condensates,” *Phys. Rev. Lett.* **96**, 097005 (2006).

- [17] M. Dzero, E.A. Yuzbashyan, B.L. Altshuler, and P. Coleman, “Spectroscopic signatures of nonequilibrium pairing in atomic Fermi gases,” *Phys. Rev. Lett.* **99**, 160402 (2007).
- [18] R.G. Scott, F. Dalfovo, L.P. Pitaevskii, and S. Stringari, “Rapid ramps across the BEC-BCS crossover: A route to measuring the superfluid gap,” *Phys. Rev. A* **86**, 053604 (2012).
- [19] G. Bruun, “Long-lived Higgs mode in a two-dimensional confined Fermi system,” *Phys. Rev. A* **90**, 023621 (2014).
- [20] S. Hannibal, P. Kettmann, M. D. Croitoru, A. Vagov, V. M. Axt, and T. Kuhn, “Quench dynamics of an ultracold Fermi gas in the BCS regime: Spectral properties and confinement-induced breakdown of the Higgs mode,” *Phys. Rev. A* **91**, 043630 (2015).
- [21] J. Kinast, S.L. Hemmer, M.E. Gehm, A. Turlapov, and J.E. Thomas, “Evidence for superfluidity in a resonantly interacting Fermi gas,” *Phys. Rev. Lett.* **92**, 150402 (2004).
- [22] J. Kinast, A. Turlapov, and J.E. Thomas, “Breakdown of hydrodynamics in the radial breathing mode of a strongly interacting Fermi gas,” *Phys. Rev. A* **70**, 051401 (2004).
- [23] M. Bartenstein, A. Altmeyer, S. Riedl, S. Jochim, C. Chin, J. H. Denschlag, and R. Grimm, “Collective excitations of a degenerate gas at the BEC-BCS crossover,” *Phys. Rev. Lett.* **92**, 203201 (2004).
- [24] A. Altmeyer, S. Riedl, M. J. Wright, C. Kohstall, J. H. Denschlag, and R. Grimm, “Dynamics of a strongly interacting Fermi gas: The radial quadrupole mode,” *Phys. Rev. A* **76**, 033610 (2007).
- [25] A. Altmeyer, S. Riedl, C. Kohstall, M. J. Wright, R. Geursen, M. Bartenstein, C. Chin, J. H. Denschlag, and R. Grimm, “Precision measurements of collective oscillations in the BEC-BCS crossover,” *Phys. Rev. Lett.* **98**, 040401 (2007).
- [26] S. Riedl, E. R. Sánchez Guajardo, C. Kohstall, A. Altmeyer, M. J. Wright, J. H. Denschlag, R. Grimm, G. M. Bruun, and H. Smith, “Collective oscillations of a Fermi gas in the unitarity limit: Temperature effects and the role of pair correlations,” *Phys. Rev. A* **78**, 053609 (2008).
- [27] M. A. Baranov and D. S. Petrov, “Low-energy collective excitations in a superfluid trapped Fermi gas,” *Phys. Rev. A* **62**, 041601 (2000).
- [28] G. M. Bruun and B. R. Mottelson, “Low energy collective modes of a superfluid trapped atomic Fermi gas,” *Phys. Rev. Lett.* **87**, 270403 (2001).
- [29] G. M. Bruun, “Low-energy monopole modes of a trapped atomic Fermi gas,” *Phys. Rev. Lett.* **89**, 263002 (2002).
- [30] H. Hu, A. Minguzzi, X. J. Liu, and M. P. Tosi, “Collective modes and ballistic expansion of a Fermi gas in the BCS-BEC crossover,” *Phys. Rev. Lett.* **93**, 190403 (2004).
- [31] H. Heiselberg, “Collective modes of trapped gases at the BEC-BCS crossover,” *Phys. Rev. Lett.* **93**, 040402 (2004).
- [32] S. Stringari, “Collective oscillations of a trapped superfluid Fermi gas near a Feshbach resonance,” *Europhys. Lett.* **65**, 749–752 (2004).
- [33] M. Grasso, E. Khan, and M. Urban, “Temperature dependence and finite-size effects in collective modes of superfluid-trapped Fermi gases,” *Phys. Rev. A* **72**, 043617 (2005).
- [34] A. Korolyuk, J. J. Kinnunen, and P. Törmä, “Density response of a trapped Fermi gas: A crossover from the pair vibration mode to the Goldstone mode,” *Phys. Rev. A* **84**, 033623 (2011).
- [35] L. W. Clark, L. C. Ha, C. Y. Xu, and C. Chin, “Quantum dynamics with spatiotemporal control of interactions in a stable Bose-Einstein condensate,” *Phys. Rev. Lett.* **115**, 155301 (2015).
- [36] P. De Gennes, *Superconductivity of metals and alloys* (Addison-Wesley New York, 1989).
- [37] S. Datta and P. F. Bagwell, “Can the Bogoliubov-de Gennes equation be interpreted as a one-particle wave equation?” *Superlattices and Microstruct.* **25**, 1233–1250 (1999).
- [38] R. D. Lord, “Some integrals involving Hermite polynomials,” *Journal of the London Mathematical Society* **1**, 101–112 (1949).
- [39] A.A. Shanenko, M. D. Croitoru, A.V. Vagov, V.M. Axt, A. Perali, and F.M. Peeters, “Atypical BCS-BEC crossover induced by quantum-size effects,” *Phys. Rev. A* **86**, 033612 (2012).
- [40] Akash Jain, “Theory of non-abelian superfluid dynamics,” *Phys. Rev. D* **95**, 121701 (2017).
- [41] Emil A. Yuzbashyan, Maxim Dzero, Victor Gurarie, and Matthew S. Foster, “Quantum quench phase diagrams of an s-wave BCS-BEC condensate,” *Physical Review A* **91**, 033628 (2015).
- [42] J. Stewart, J. Gaebler, and D. Jin, “Using photoemission spectroscopy to probe a strongly interacting Fermi gas,” *Nature* **454**, 744–747 (2008).
- [43] J.T. Stewart, J.P. Gaebler, T.E. Drake, and D.S. Jin, “Verification of universal relations in a strongly interacting Fermi gas,” *Phys. Rev. Lett.* **104**, 235301 (2010).
- [44] W. Ketterle and M. Zwierlein, “Making, probing and understanding ultracold Fermi gases,” *ArXiv* (2008).